

A Model of Aerobic and Anaerobic Metabolism in Cancer Cells – Parameter Estimation, Simulation, and Comparison with Experimental Results

Svein H. Stokka¹ Eivind S. Haus¹ Gunhild Fjeld² Tormod Drenngstig¹ Kristian Thorsen¹

¹Department of Electrical Engineering and Computer Science, University of Stavanger, Norway, {svein.h.stokka, eivind.haus, tormod.drenngstig, kristian.thorsen}@uis.no

²Stavanger University Hospital, Stavanger, Norway, gunhild.fjeld@sus.no

Abstract

We present a mathematical model of metabolism in cancer cells that is capable of describing both aerobic oxidative metabolism and anaerobic fermentation metabolism, and how cancer cells shift between these metabolic states when exposed to different substrates and different enzymatic inhibitors. The model is designed to be used in combination with experimental data gathered with an Agilent Seahorse XF metabolic analyzer. The model is parameterized in a manual tuning procedure to fit experimental data, and validated against experimental data from another setup, to which the model shows good conformity. We also investigate the structural identifiability of the model. The results indicate that the model is structurally identifiable, and that it can thus be uniquely parameterized, using the following 5 measurements: extracellular concentrations of glucose, glutamine and lactate, proton production rate (a Seahorse XF analyzer measurement) and oxygen consumption rate.

Keywords: biological systems, cancer metabolism, simulation, parameter estimation, biotechnology

1 Introduction

Cancer is a group of diseases where cells grow and proliferate uncontrollably (Jones and Thompson, 2009). An emerging hallmark of cancer is reprogrammed energy metabolism (Hanahan and Weinberg, 2011). Metabolism is important in understanding how different cancer cells proliferate and develop into tumors and metastases, and for designing and testing therapeutic strategies.

Cancer cells differ from non-cancerous cells in that they typically have a high uptake of glucose and a shift from energetically efficient oxidative metabolism to less efficient anaerobic fermentation even in the presence of O₂. This phenomenon is the so-called Warburg effect (Liberti and Locasale, 2016; Warburg, 1956). Many cancer cells also have an increased metabolic reliance on glutamine (Wise and Thompson, 2010), which is the most abundant free amino acid in muscles and blood plasma.

In this paper we present a model of aerobic and anaerobic metabolism in cancer cells designed to be used in

combination with experiments performed using an Agilent Seahorse XF analytic instrument, a commonly used tool for studying and metabolic phenotyping cancer cells. The Seahorse XF instrument measures oxygen consumption rate (OCR) and extracellular acidification rate (ECAR) in live cells under controlled conditions. The instrument features automatic injection and mixing of up to four substances and can run experiments that reveal how cells respond to addition of metabolic substrates and how they respond to forced blocking of certain metabolic pathways by the addition of enzymatic inhibitors (Agilent, 2019).

2 Modeling

Our model includes cellular uptake and metabolism of glucose and glutamine, and describes the most prominent metabolic processes by simplified kinetic expressions. The model deals with enzymatic reactions, i.e. fast changes in metabolic reaction rates, due to immediate additions of substrates and inhibitors. Since the timescale of experiments are in the order of minutes to a maximum of a few hours, significantly shorter than the doubling time for typical cell lines used in these experiments, cell growth is not considered in the model. The Caco2 cell line used in this work has a doubling time in the range of days (Hidalgo et al., 1989). Figure 1 shows a schematic overview of the model (see also Table 1 for a list of abbreviations). The model has the following 12 state variables: the internal concentrations of metabolites and metabolic intermediates (glucose, pyruvate, glutamine, α -ketoglutarate, and lactate), the internal concentration of ADP and ATP (for energy production and balance), the concentration of NAD⁺ and NADH (the electron carrier in oxidative production of ATP), and the external concentrations of glucose, glutamine, and lactate. There are in total 11 metabolic reactions, or flow expressions, in the model. As indicated by the red and green symbols in Figure 1, the model also includes the effect of the following 5 inhibitors: 2-DG (2-deoxyglucose), rotenone, antimycin A, oligomycin and CCCP (Carbonyl cyanide m-chlorophenyl hydrazone). These inhibitors are often used in Seahorse experiments, such as glycolysis- and mitochondrial stress tests (Agilent, 2019).

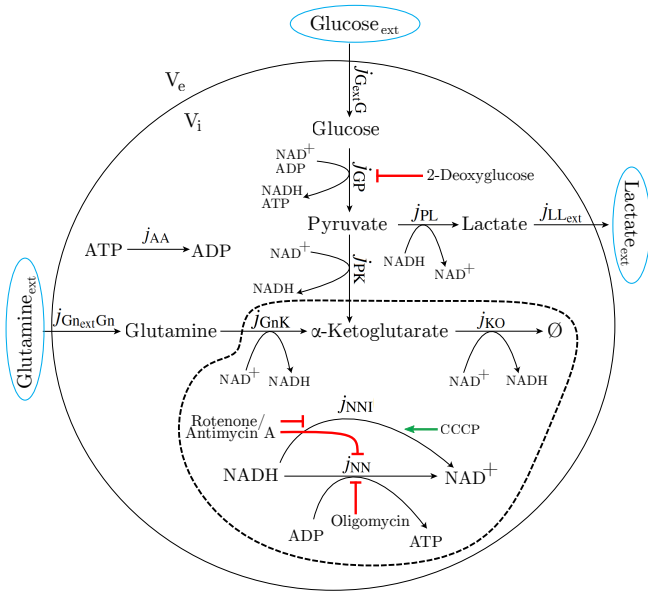


Figure 1. Overview of the model. The fully drawn circle is the cell membrane. Inside the dotted line is the mitochondria. The black arrows are metabolic reactions and the red and green lines show inhibitors/activators often used in Seahorse experiments.

Notation

The reactions in the model are simplified and each reaction actually covers multiple enzyme catalyzed reaction steps. Unless otherwise stated, we assume that the overall reactions are irreversible and we use the rate constants k to describe the maximum reaction- or transport rate. We use subscript to denote the reaction, e.g., the rate constant for glycolysis, j_{GP} , is k_{GP} . The effect of substrates in reactions are expressed by saturation ratios r ($0 \leq r \leq 1$), where we use subscript to denote the reaction and superscript to denote the substrate. We use saturation ratios based on the Michaelis-Menten equation. As an example, the contribution of glucose G to the glycolysis rate j_{GP} is described in the saturation ratio given as $r_{GP}^G = \frac{G}{K_{GP}^G + G}$, where K_{GP}^G is the half-saturation constant.

The expressions for the different reactions in the model will be explained in the following.

Transport

With a few exceptions, such as O_2 and CO_2 , most molecules cannot freely diffuse across the cell membrane, and thus, transport across the cell membrane is dependent on transport proteins. Glucose is transported across the cell membrane by glucose transporter proteins (SLC2A family) through facilitated diffusion – a passive process where the concentration gradient provides energy for protein mediated transport across the membrane. The so-called GLUT1 transporter protein (SLC2A1) is of special interest in studies of cancer metabolism, as it is abundant in many human tumor types (DeBerardinis et al., 2008; Hanahan and Weinberg, 2011).

Glutamine is transported across the cell membrane

Table 1. List of abbreviations.

G	glucose
P	pyruvate
Gn	glutamine
K	α -ketoglutarate
L	lactate
NAD^+	nicotinamide adenine dinucleotide (oxidized form)
NADH	nicotinamide adenine dinucleotide (reduced form)
ATP	adenosine triphosphate
ADP	adenosine diphosphate
G_{ext}	extracellular glucose
Gn_{ext}	extracellular glutamine
L_{ext}	extracellular lactate
OCR	oxygen consumption rate
ECAR	extracellular acidification rate
PPR	proton production rate
TCA cycle	tricarboxylic acid cycle
2-DG	2-deoxyglucose

by several amino acid transporters, but most notably by SLC1A5 and SLC6A14 which are commonly upregulated in cancer cells (Scalise et al., 2017; Cha et al., 2018).

Lactate is transported out of the cell by monocarboxylate transporters (MCTs), a type of symporter that couple protons (H^+) and monocarboxylate transport, and hence, lactate excretion is coupled with extracellular acidification.

The expressions for transport of glucose, glutamine and lactate in Eqs.(1)-(3) respectively, are all modeled as facilitated diffusion through transporter proteins where we use the fixed site carrier model (Baker and Widdas, 1973) describing transport through a membrane pore with binding sites on both sides of the membrane.

$$j_{G_{ext}G} = k_{G_{ext}G} \frac{G_{ext} - G}{\left(K_{G_{ext}G}^{G_{ext}} + G_{ext}\right) \left(K_{G_{ext}G}^G + G\right)} \quad (1)$$

$$j_{Gn_{ext}Gn} = k_{Gn_{ext}Gn} \frac{Gn_{ext} - Gn}{\left(K_{Gn_{ext}Gn}^{Gn_{ext}} + Gn_{ext}\right) \left(K_{Gn_{ext}Gn}^{Gn} + Gn\right)} \quad (2)$$

$$j_{LL_{ext}} = k_{LL_{ext}} \frac{L - L_{ext}}{\left(K_{LL_{ext}}^L + L\right) \left(K_{LL_{ext}}^{L_{ext}} + L_{ext}\right)} \quad (3)$$

The transport of glucose ($j_{G_{ext}G}$) and glutamine ($j_{Gn_{ext}Gn}$) are defined positive into the cell, whereas the transport of lactate ($j_{LL_{ext}}$) is defined positive out of the cell.

Glycolysis and fermentation

Glucose is converted to pyruvate in a series of 10 enzyme catalyzed reactions in the glycolysis pathway. The net production for each glucose molecule through the glycolysis is 2 pyruvate-, 2 ATP- and 1 NADH molecules. The modeled expression for the glycolytic flux, j_{GP} , given as

$$j_{GP} = k_{GP} r_{GP}^G r_{GP}^{ADP} r_{GP}^{NAD} \quad (4)$$

depend on glucose, ADP and NAD^+ .

Cells regenerate NAD^+ to sustain glycolysis, and if O_2 is available most cells prefer to oxidize NADH in the mitochondria to produce more ATP. In the absence of O_2 , cells regenerate NAD^+ through fermentation by reducing pyruvate to lactate. Cancer cells, however, often show a preference for fermentation even in the presence of O_2 , which refers to the so-called Warburg effect or aerobic glycolysis. The expression for fermentation, j_{PL} , is given as

$$j_{\text{PL}} = k_{\text{PL}} r_{\text{PL}}^{\text{P}} r_{\text{PL}}^{\text{NADH}} \quad (5)$$

Oxidative metabolism

In the mitochondria (the inside of the dashed line in Figure 1) organic material such as pyruvate can be further catabolized in the TCA cycle (tricarboxylic acid cycle) to produce large quantities of NADH, which is oxidized to NAD^+ by O_2 in the electron transport chain. The oxidation of NADH is coupled to ATP production by a proton gradient across the inner mitochondrial membrane, where the gradient is sustained by proton transport by the electron transport chain and used by ATP synthase to produce ATP. This process is called oxidative phosphorylation. To account for proton leak, we use the following two fluxes to describe oxidative phosphorylation.

$$j_{\text{NN}} = k_{\text{NN}} r_{\text{NN}}^{\text{NADH}} r_{\text{NN}}^{\text{ADP}} \quad (6)$$

$$j_{\text{NNI}} = k_{\text{NNI}} \text{NADH} \quad (7)$$

where j_{NN} describe the regeneration of NAD^+ coupled to ATP production and j_{NNI} describe the regeneration of NAD^+ coupled to proton leak across the membrane.

Pyruvate is transported into the mitochondria where it is completely catabolized in the TCA cycle producing 4 NADH molecules for each pyruvate molecule. In the model we describe the catabolism of pyruvate in two steps: first conversion of pyruvate to TCA intermediate α -ketoglutarate, j_{PK} in equation (8), and second conversion of α -ketoglutarate to oxaloacetate, j_{KO} in equation (9).

In addition, glutamine enters the TCA cycle through glutaminolysis, j_{GnK} in equation (10), where glutamine is converted to α -ketoglutarate that also produce NAD(P)H. Oxaloacetate is in the model treated as a sink (symbol \emptyset in Figure 1) as we do not include further anabolic processes.

$$j_{\text{PK}} = k_{\text{PK}} r_{\text{PK}}^{\text{P}} r_{\text{PK}}^{\text{NAD}} \quad (8)$$

$$j_{\text{KO}} = k_{\text{KO}} r_{\text{KO}}^{\text{K}} r_{\text{KO}}^{\text{NAD}} \quad (9)$$

$$j_{\text{GnK}} = k_{\text{GnK}} r_{\text{GnK}}^{\text{Gn}} r_{\text{GnK}}^{\text{NAD}} \quad (10)$$

Energy consumption

We assume that the cellular energy consumption, j_{AA} , depends on ATP availability as follows:

$$j_{\text{AA}} = k_{\text{AA}} r_{\text{AA}}^{\text{ATP}} \quad (11)$$

State equations

Equations (1) - (11) represent the 11 reactions in our model, giving the following 12 state equations of our model:

$$\dot{G} = j_{\text{GextG}} - j_{\text{GP}} \quad (12)$$

$$\dot{P} = 2j_{\text{GP}} - j_{\text{PK}} - j_{\text{PL}} \quad (13)$$

$$\dot{\text{Gn}} = j_{\text{GnextGn}} - j_{\text{GnK}} \quad (14)$$

$$\dot{K} = j_{\text{PK}} + j_{\text{GnK}} - j_{\text{KO}} \quad (15)$$

$$\dot{L} = j_{\text{PL}} - j_{\text{LLext}} \quad (16)$$

$$\begin{aligned} \dot{\text{NAD}} &= j_{\text{PL}} + j_{\text{NN}} + j_{\text{NNI}} - j_{\text{GnK}} \\ &\quad - 2j_{\text{GP}} - 2j_{\text{PK}} - 2j_{\text{KO}} \end{aligned} \quad (17)$$

$$\dot{\text{NADH}} = -\dot{\text{NAD}} \quad (18)$$

$$\dot{\text{ATP}} = 2j_{\text{GP}} + 2.5j_{\text{NN}} - j_{\text{AA}} \quad (19)$$

$$\dot{\text{ADP}} = -\dot{\text{ATP}} \quad (20)$$

$$\dot{n}_{\text{Gext}} = -V_i j_{\text{GextG}} \quad (21)$$

$$\dot{n}_{\text{Gnext}} = -V_i j_{\text{GnextGn}} \quad (22)$$

$$\dot{n}_{\text{Lext}} = V_i j_{\text{LLext}} \quad (23)$$

where V_i is the total cellular volume. Note that the extracellular state variables are expressed in amount in moles instead of concentration because the extracellular volume may change. The extracellular concentration of glucose, glutamine and lactate are found by dividing their respective amount by the extracellular volume V_e .

3 Seahorse XF

The Seahorse XFp Analyzer measures OCR and ECAR on live cells placed in a specialized well plate. The measurements are performed by sinking a sensor into the well creating a microchamber with a volume of $2\mu\text{l}$ where changes in pH and O_2 concentration occur more rapidly due to the small volume.

ECAR measurements, which is the change of pH in the microchamber ($-\frac{dpH}{dt}$), are converted to PPR (proton production rate), which is a measure of the number of protons (H^+) excreted from the cells. Excretion of lactate is the primary source of extracellular acidification and is related to PPR (mol/s) by

$$\text{PPR} = V_i j_{\text{LLext}} \quad (24)$$

OCR is a measurement of cellular O_2 consumption, ($-\frac{d\text{O}_2}{dt}$), where oxidation of NADH in oxidative phosphorylation is the primary consumer of O_2 . Since 2 NADH molecules is oxidized for each O_2 molecule, OCR (mol/s) is related to oxidative phosphorylation by

$$\text{OCR} = \frac{V_i}{2} (j_{\text{NN}} + j_{\text{NNI}}) \quad (25)$$

Inhibitors

The model is designed to be used in combination with experimental results from so called glycolysis- and mitochondrial stress tests performed with the Seahorse XFp

Analyzer. In these experiments, inhibitors that block or disrupt certain metabolic pathways in the cells are injected into the wells. The following describe these inhibitors and how we implement their effect in the model.

2-Deoxyglucose (2-DG) is a glucose analogue that is transported through the cell membrane by GLUT1. Inside the cell 2-DG and its derivatives inhibit early steps in glycolysis, j_{GP} . We implement the injection of 2-DG as a 99% decrease in the rate constant for glycolysis, k_{GP} .

Oligomycin is an inhibitor of the enzyme complex ATP synthase, which phosphorylate ADP in oxidative phosphorylation, and we implement the injection of oligomycin as a decrease in the rate constant k_{NN} by 99%. Oxidation of NADH still occurs, but at a lower rate, primarily due to proton leak across the mitochondrial inner membrane, which is described by j_{NNI} .

CCCP is an inhibitor of oxidative phosphorylation, i.e. it uncouples the oxidation of NADH with ATP synthesis by destroying the proton gradient across the inner mitochondrial membrane and therefore acts as an activator of oxidative phosphorylation coupled to proton leak. We implement the injection of CCCP as an increase in the rate constant for the oxidation of NADH coupled to proton leak k_{NNI} . The factor of increase is a tuning parameter during parameter estimation, where we initially increase k_{NNI} by a factor of 100.

Rotenone and antimycin A inhibit oxidative phosphorylation by limiting the oxidation of NADH. We implement the effect of these inhibitors as a 99% decrease in the rate constants for oxidative phosphorylation k_{NN} and k_{NNI}

4 Parameter estimation

The model was fitted to experimental data from a glycolysis stress test, a method that measures key properties of the glycolytic pathway, in a manual parameter tuning procedure. We performed the experimental test on cancer cells from the cancer cell line Caco2 (Hidalgo et al., 1989). In the test the cells are initially starved for glucose, but glutamine is available in the media. The Seahorse XFp Analyzer then sequentially adds: (i) glucose, starting glycolytic activity, (ii) oligomycin, inhibiting mitochondrial ATP production in oxidative phosphorylation and thereby increasing glycolytic activity to maximal capacity, (iii) CCCP, further inhibiting oxidative phosphorylation, and (iv) 2-DG, inhibiting glycolysis. Initial media volume in the wells, the extracellular volume V_e , is $180 \mu\text{l}$ and for each injection the volume increase by $25 \mu\text{l}$. The cell culture contained an estimate of 15000 cells, which based on average cell size for Caco2 cells (Hidalgo et al., 1989), correspond to a total cell volume V_i of $0.0204 \mu\text{l}$.

The possible ranges of the reaction fluxes in the model were calculated from OCR and PPR measurements based on the stoichiometry. Prior to glucose injection, glucose uptake is restricted since glucose is not available in the media and therefore glucose uptake $j_{G_{\text{ext}}G}$ is zero. By assuming that oligomycin and 2-DG completely inhibit ATP

coupled oxidative phosphorylation and glycolysis respectively, further restrictions on fluxes were possible; j_{NN} was set to zero after oligomycin injection and j_{GP} was set to zero after 2-DG injection.

In order to identify a set of initial model parameters, we use the glucose phase which is after the addition of glucose but prior to the addition of inhibitors. Having both glucose and glutamine present in the growth media is common in experiments, and thus, it enables us to use available literature data, see Table 2. To obtain stationary conditions in the model, external concentrations of glucose, glutamine and lactate were considered constant and the differential equations were solved for the rate constants. Uptake of glucose $j_{G_{\text{ext}}G}$ and glutamine $j_{G_{\text{ext}}Gn}$, excretion of lactate $j_{LL_{\text{ext}}}$ and ATP coupled oxidative phosphorylation j_{NN} were considered known in the calculation since they are the easiest fluxes to measure or estimate from OCR and PPR. We use $j_{G_{\text{ext}}G} = 2.26 \text{mM/min}$, $j_{G_{\text{ext}}Gn} = 3.47 \text{mM/min}$, $j_{LL_{\text{ext}}} = 4.25 \text{mM/min}$ and $j_{NN} = 10.4 \text{mM/min}$. As a starting point the saturation ratios r were set to $\frac{1}{2}$, which is equivalent to setting the half-saturation constants K equal to their respective substrate concentrations in Table 2.

Table 2. Assumed steady state concentration (SS [mM]) after glucose injection. These values are used in the manual tuning procedure. *Obtained from (Shestov et al., 2014). **Experimental setup.

G	5	K	1	NADH	0.1	G_{ext} **	10.0
P*	0.5	L	0.5	ATP*	3.0	Gn_{ext} **	0.2
Gn	0.1	NAD*	0.5	ADP	1	L_{ext}	0.1

Manual tuning

With the initial parameter set (Table 3), we simulated the model and compared it to measurements of OCR and PPR, see Figure 2, panel A. We see that the model poorly captures the dynamics, especially PPR in phases 3-5.

As a measure to improve the model, we decreased K_{GP}^{NAD} and K_{PL}^{NADH} significantly; in such a way that glycolysis and fermentation became saturated with NAD^+ and NADH, respectively, causing PPR to increase as response to oligomycin and CCCP injection, see phases 3 and 4 of panel B. The increased rate of glycolysis from saturated NAD^+ was compensated for by reducing the rate constant for glycolysis k_{GP} by a factor of 2. It was not necessary to compensate the rate of fermentation, as it is limited by glycolysis, and most pyruvate is already fermented to lactate, i.e. the flux from pyruvate to α -ketoglutarate is small.

We observe that the model response in panel B is improved compared to panel A. In order to further improve the model response with respect to proton leak (OCR) before CCCP injection (phase 1-3), we adjusted the rate constant k_{NNI} until the model response fitted the experimental results in phase 3. This is a well suited tuning method as oxidative phosphorylation coupled to ATP production, j_{NN} , is inhibited in phase 3.

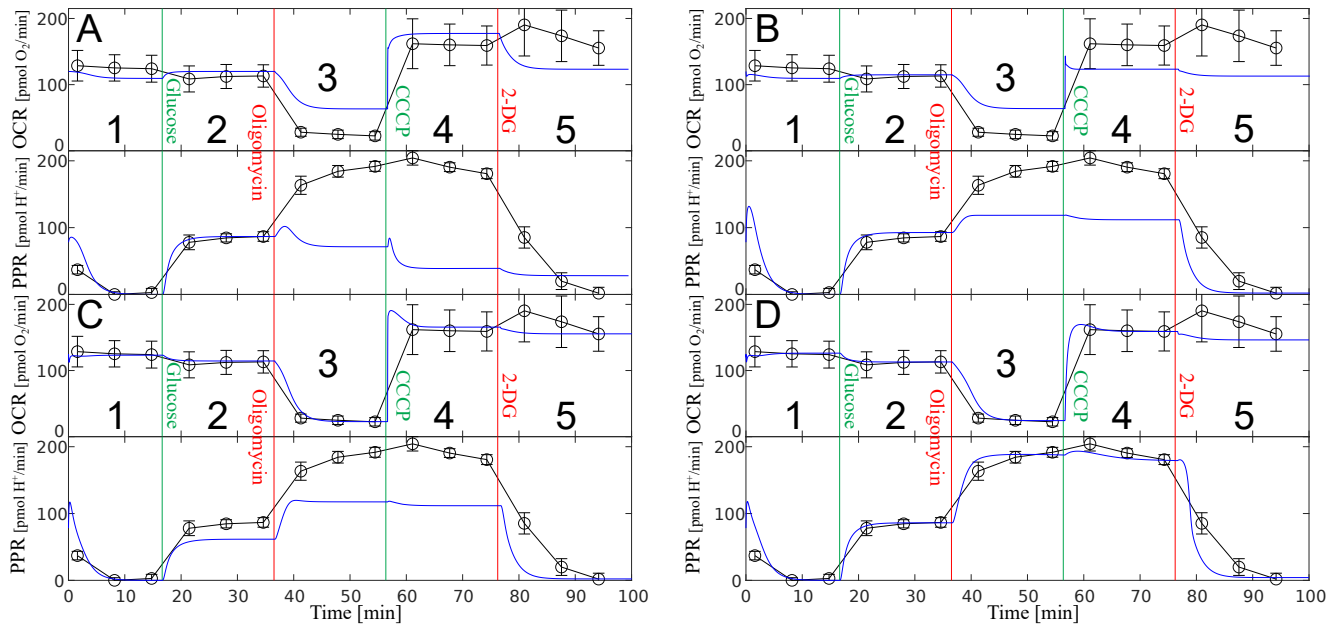


Figure 2. Simulation (blue) and experimental measurements (black) of oxygen consumption rate (OCR) and proton production rate (PPR calculated from ECAR) for the parameter estimation procedure. Injections of glucose and metabolic inhibitors shown on vertical lines. **A** Simulation based on the initial parameter set, see main text. **B** Glycolysis and fermentation were saturated with NAD^+ and NADH respectively to increase PPR as a response to oligomycin and CCCP injection. The increased glycolytic flux from this adjustments was compensated. **C** Oxidative phosphorylation coupled to proton leak prior to CCCP injection was adjusted so it described OCR after oligomycin injection. Glutaminolysis and the energy consumption rate was adjusted so that it better described the glucose injection. **D** Response after last adjustments. Glycolysis was increased until PPR coincided with experimental data after oligomycin injection. The increased glycolytic flux after glucose injection was compensated by reducing ADP availability through increasing oxidative phosphorylation coupled to ATP production. As a last step the effect of CCCP on oxidative phosphorylation coupled to proton leak was adjusted until OCR after CCCP injection coincided with experimental data.

We also observe that after glucose addition (panel B, phase 2), the model response of OCR is opposite of the experimental results. To improve this response, we increased the rate of glutaminolysis k_{GnK} and decreased the energy consumption rate k_{AA} , see panel C. This adjustment of the energy consumption rate was necessary both to decrease the rate of glutaminolysis and glycolysis, and to shift the glucose metabolism towards fermentation in phase 2.

The response in panel C shows a relative good fit to the experiment in OCR but a not so good fit in PPR. To improve the PPR response in phases 3 and 4, we increased the rate for glycolysis k_{GP} to ensure that glucose is fermented to lactate at maximal capacity after oligomycin injection (phase 3). As this adjustment also increase the rate of glycolysis during phase 2, were the PPR became too high, an increase in the rate of oxidative phosphorylation coupled to ATP production k_{NN} was necessary. Furthermore, to improve the OCR response in phase 4 after the addition of CCCP, we decreased k_{NNI} once again, this time however, we changed the value of k_{NNI} when it is affected by CCCP.

The resulting simulation after tuning, shown in panel D, shows a good fit with the experimental data, especially considering that only 8 parameters were adjusted during the manual tuning. Parameter values before and after tuning are listed in Table 3. However, in phase 3 after the ad-

dition of oligomycin, the response is too fast with respect to PPR, and too slow with respect to OCR. This is possibly a result of not including compartmentalization in the model, resulting in increased ADP availability in the mitochondria from inhibition of ATP synthase by oligomycin, immediately affecting the glycolysis in the model.

The rapid increase and peak in OCR after CCCP injection in phase 4 is in the model caused by rapid depletion of accumulated α -ketoglutarate after oligomycin injection, i.e. it signifies accumulation of TCA intermediates in the cells. Similarly, the small transient increase in PPR from CCCP injection is in the model a result of accumulation of lactate after the preceding oligomycin injection. This is due to saturation in lactate excretion where increased external volume from the injection of CCCP is associated with dilution of external lactate, which increases the concentration gradient and therefore allows a higher flux.

The experimental data show a transient increase in OCR after injection of 2-DG in phase 5, which is not captured by the model; it is not clear why this transient occurs.

Validation

To validate the model and parameters identified through the glycolysis stress test, we compared the model with experimental data from a so-called mitochondrial stress test which measures key properties for mitochondrial respiration. We used the same cell line Caco2 with the same

Table 3. Estimated parameter values. Rate constants k [mM/s] and half saturation constants (K) in [mM]. For parameters that were adjusted in the manual tuning both the initial- and final estimates are included. * k_{NNI} when CCCP is present.

Par	Value	Par	Value	Par	Value
$K_{\text{G}_{\text{ext}}\text{G}}^{\text{G}_{\text{ext}}}$	10	$K_{\text{LL}_{\text{ext}}}^{\text{L}_{\text{ext}}}$	0.1	$K_{\text{GnK}}^{\text{Gn}}$	0.1
$K_{\text{G}_{\text{ext}}\text{G}}^{\text{G}}$	5	$k_{\text{L}_{\text{ext}}\text{L}}$	0.0354	$K_{\text{GnK}}^{\text{NAD}}$	0.5
$k_{\text{G}_{\text{ext}}\text{G}}$	1.508	K_{PK}^{P}	0.5	K_{KO}^{K}	1
K_{GP}^{G}	5	$K_{\text{PK}}^{\text{NAD}}$	0.5	$K_{\text{KO}}^{\text{NAD}}$	0.5
$K_{\text{GP}}^{\text{ADP}}$	1	k_{PK}	0.018	k_{KO}	0.2493
K_{PL}^{P}	0.5	$K_{\text{Gn}_{\text{ext}}\text{Gn}}^{\text{Gn}_{\text{ext}}}$	0.2	$K_{\text{NN}}^{\text{NADH}}$	0.1
k_{PL}	0.2833	$K_{\text{Gn}_{\text{ext}}\text{Gn}}^{\text{Gn}}$	0.1	$K_{\text{NN}}^{\text{ADP}}$	1
$K_{\text{LL}_{\text{ext}}}^{\text{L}}$	0.5	$k_{\text{Gn}_{\text{ext}}\text{Gn}}$	0.04624	$K_{\text{AA}}^{\text{ATP}}$	3

Par	Initial	Final	Par	Initial	Final
$K_{\text{GP}}^{\text{NAD}}$	0.5	0.001	$K_{\text{PL}}^{\text{NADH}}$	0.1	0.001
k_{GP}	0.3013	0.377	k_{GnK}	0.2313	0.37
k_{AA}	1.0173	0.865	k_{NN}	0.693	1.11
k_{NNI}	0.2267	0.057	* k_{NNI}	22.67	1.995

number of cells as in the glycolysis stress test. The media in the mitochondrial stress test contain glutamine and glucose, but at a lower concentration (5mM) than after the glucose injection in the glycolysis stress test (10mM). The Seahorse XFp Analyzer sequentially adds (i) oligomycin, (ii) CCCP, (iii) Rotenone and (iv) antimycin A. The last two are new compared to the glycolysis stress test, and they both inhibit oxidative phosphorylation.

The simulation and the experimental data from the mitochondria stress test is shown in Figure 3 and shows a remarkable good fit. The relatively unaffected PPR response (both experimentally and simulated) is expected since all the injections inhibit oxidative phosphorylation and fermentation operate at maximal capacity to sustain glycolysis for energy production.

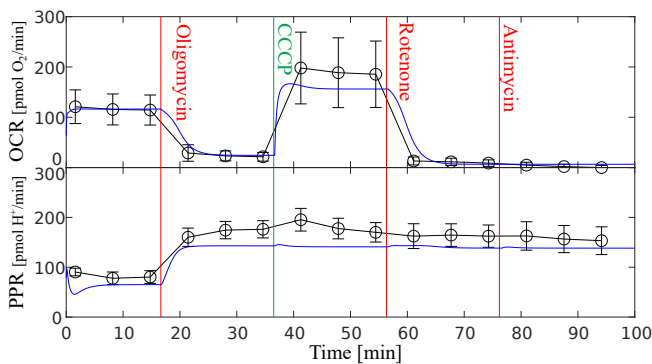


Figure 3. Simulation (blue) and experimental measurements (black) of oxygen consumption rate (OCR) and proton production rate (PPR calculated from ECAR) for a mitochondrial stress test. Injections of metabolic inhibitors shown on vertical lines.

5 Structural properties

Intrigued by the model's ability to fit the experimental results and to capture the main dynamics, we wanted to examine the structural properties of the model in more detail. We wanted to investigate the possibilities for using an automated method for parametrization. Thus we needed to see if the model could be uniquely parameterized from available data and chose to look at the *structural identifiability* of the model.

In this context, the number of measurements are of importance. Adding more measurements to the experimental setup, especially substances inside the cell, like internal concentrations of metabolites, will increase the experimental complexity and cost. We therefore wanted to explore whether the Seahorse measurements (PPR and OCR) together with the external concentrations of glucose, glutamine and lactate form a sufficient set of measured outputs for parameter identifiability.

Structural identifiability

We will first briefly explain the concept of structural identifiability. A model based on a general non-linear state space form: $\frac{dx(t)}{dt} = f(x(t), u(t), \theta)$ and $y(t) = h(x(t), u(t), \theta)$ is identifiable if all parameters θ can be uniquely determined from the system input $u(t)$ and the measured system output $y(t)$ (Miao et al., 2011). A generic form of identifiability is structural identifiability, where the term *structural* indicates that it depends solely on the model structure, i.e. structural identifiability is completely determined by the structure of the system equations and the output function (Villaverde, 2019). For a model to be structurally identifiable, all of its parameters must be structurally identifiable. If this is not the case, it is structurally unidentifiable. If a model is found to be structurally identifiable with a chosen set of measured outputs, it is theoretically possible to uniquely estimate the parameters of the model based on these measurements.

Method

Over time a variety of methods to investigate structural identifiability have been suggested. Some examples are analytic approaches using Taylor series or similarity transformation (Chis et al., 2011; Miao et al., 2011). One major weakness of these and other analytic methods are that the resulting set of non-linear equations can be computationally difficult to solve because of their complexity. Given the amount of parameters in our model, this would be the case for us. Therefore we chose a method suggested and used by Stigter et al. in (2015), (2017), (2018). This method is designed for use on models with many parameters and uses a hybrid numerical and symbolic approach.

With this method the model is simulated with parameter values randomly chosen within a constrained box of realistic parameter values. This is repeated 10 times to ensure robustness. A set of singular values and a set of correlated parameters θ_{corr} are calculated from these simu-

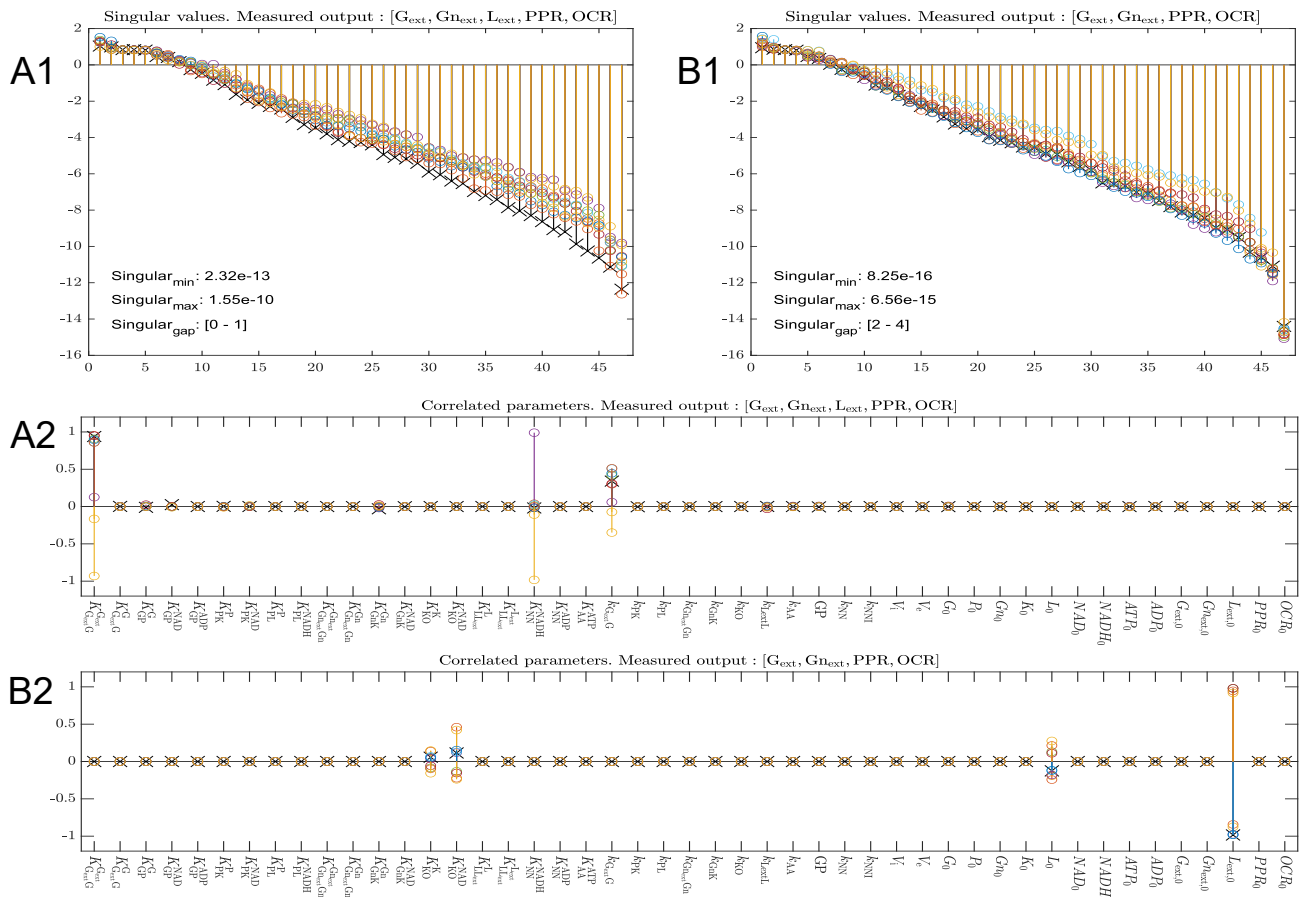


Figure 4. **A1** Log scale plot of singular values. No discernible gap between the smallest singular values indicates structural identifiability. **B1** Log scale plot of singular values without measurement of external lactate L_{ext} . Singular values 10^3 orders of magnitude smaller than panel A1 and a defined gap indicates structural unidentifiability. **A2** Plot of correlated parameters related to panel A1. This plot does not give any relevant information when the model is structurally identifiable. **B2** Plot of correlated parameters related to panel B1. From the plot we see that the parameters $[K_{LL_{ext}}^L, K_{LL_{ext}}^{L_{ext}}, L_0, L_{ext}]$ are correlated.

lations. The singular values, or more specifically a prominent jump in numerical value of the lowest singular values, will indicate whether the model is structurally unidentifiable, while the set of correlated parameters will indicate which parameters are causing this structural unidentifiability. A symbolic calculation with this reduced set of parameters θ_{corr} can then be performed to confirm the results indicated by the simulations. For a more in depth explanation of the method see (Stigter and Molenaar, 2015).

Experiments and results

In addition to the 12 states of the model, we add PPR and OCR as states to be used as measured outputs in the algorithm. The model has a total of 47 parameters, including 20 half saturation constants, 11 rate constants, internal and external volume, and the initial conditions of the 14 states.

A natural first choice of measurements are the PPR and OCR provided by the Seahorse XFp analyzer. However, they proved insufficient to obtain structural identifiability.

We included therefore the three external concentrations $[G_{ext}, Gn_{ext}, L_{ext}]$ in our measured output set as they are relatively easy to measure during an experiment. Run-

ning the algorithm with these 5 measured outputs gave the results shown in Figure 4, panels A1 and A2. Very small singular values and a clear gap, typically greater than 3 (Joubert et al., 2018), between the smallest singular values would indicate structural unidentifiability. In panel A1 we observe a gap of an order between 0 and 1, indicating structural identifiability. When a model is found to be structurally identifiable from the singular values plot, the plot of correlated parameters (such as in panel A2) does not contribute with any relevant information (even if it looks like two or more parameters are correlated). The symbolic verification supports the conclusion from the simulations.

Having a situation where measurements of OCR and PPR together with the 3 external concentrations are enough for the model to be structurally identifiable, we wanted to investigate whether we could remove one of the external concentration measurements and still obtain the same result. Thus, running the algorithm three times with one of the external measurements left out for each run resulted in all runs indicating a lack of structural identifiability. Panels B1 and B2 in Figure 4 show the results

with the measurement of external lactate L_{ext} left out. The plot of singular values in panel B1 shows that the smallest singular values are of order 10^{-15} to 10^{-16} and that there is a clear gap between the two smallest singular values. Panel B2 shows a plot of the correlated parameters for this case, i.e. $\theta_{\text{corr}} = [K_{L_{\text{ext}}}^L, K_{L_{\text{ext}}}^{L_{\text{ext}}}, L_0, L_{\text{ext}}]$. This is a reasonable result since all these parameters can be found in equation (3) describing the transport of lactate out of the cell. Performing the symbolic calculation with this reduced parameter set θ_{corr} also indicates structural unidentifiability, confirming the numerical results.

6 Conclusions

We constructed a dynamic model of aerobic and anaerobic metabolism in cancer cells designed to be used in combination with experiments performed using an Agilent Seahorse XF analytic instrument. The model consist of 12 state variables including the external concentration of glucose, glutamine and lactate and describes 2 common types of reprogrammed energy metabolism in cancer cells, i.e. aerobic glycolysis and glutamine addiction.

Parameter values were estimated based on experimental data from a glycolysis stress test on the Caco2 cell line in a manual tuning procedure. The model was then validated with experimental data from a mitochondrial stress test on the same cell line with promising results.

Our experiments indicate that the model is structurally identifiable with a set of 5 measured outputs $[G_{\text{ext}}, G_{\text{n}_{\text{ext}}}, L_{\text{ext}}, \text{PPR}, \text{OCR}]$. These are measurements that are simple to perform experimentally and that can be performed in vivo (without killing cells). However, we must keep in mind that this is a purely theoretical result and in practice it could still be difficult to uniquely parameterize the model based on only these 5 measured outputs.

For future work we will investigate an automatic method for parameterization as an alternative to manual parameter tuning. Our results from the structural identification analysis supports a possible unique parameterization with an automated algorithm.

References

Agilent. Brochure - Agilent seahorse XF live-cell metabolism solutions for cancer research, 2019. URL <https://www.agilent.com/en/solutions/cell-analysis/cell-metabolism/cancer-metabolism>.

G. F. Baker and W. F. Widdas. The asymmetry of the facilitated transfer system for hexoses in human red cells and the simple kinetics of a two component model. *The Journal of Physiology*, 231(1):143–165, 1973. doi:10.1113/jphysiol.1973.sp010225.

Y. J. Cha, E. S. Kim, and J. S. Koo. Amino acid transporters and glutamine metabolism in breast cancer. *International Journal of Molecular Sciences*, 19(3), 2018. doi:10.3390/ijms19030907.

O. T. Chis, J. R. Banga, and E. Balsa-Canto. Structural identifiability of systems biology models: A criti-

cal comparison of methods. *PLoS ONE*, 6(11), 2011. doi:10.1371/journal.pone.0027755.

R. J. DeBerardinis, J. J. Lum, G. Hatzivassiliou, and C. B. Thompson. The biology of cancer: Metabolic reprogramming fuels cell growth and proliferation. *Cell Metabolism*, 7(1):11–20, 2008. doi:10.1016/j.cmet.2007.10.002.

D. Hanahan and R. A. Weinberg. Hallmarks of cancer: The next generation. *Cell*, 144(5):646–674, 2011. doi:10.1016/j.cell.2011.02.013.

I. J. Hidalgo, T. J. Raub, and R. T. Borchardt. Characterization of the human colon carcinoma cell line (Caco-2) as a model system for intestinal epithelial permeability. *Gastroenterology*, 96(3):736–749, 1989. doi:10.1016/0016-5085(89)90897-4.

R. G. Jones and C. B. Thompson. Tumor suppressors and cell metabolism: A recipe for cancer growth. *Genes and Development*, 23(5):537–548, 2009. doi:10.1101/gad.1756509.

D. Joubert, J. D. Stigter, and J. Molenaar. Determining minimal output sets that ensure structural identifiability. *PLoS ONE*, 13(11):1–19, 2018. doi:10.1371/journal.pone.0207334.

M. V. Liberti and J. W. Locasale. The Warburg effect: How does it benefit cancer cells? *Trends in Biochemical Sciences*, 41(3):211–218, 2016. doi:10.1016/j.tibs.2015.12.001.

H. Miao, X. Xia, A. S. Perelson, and H. Wu. On identifiability of nonlinear ODE models and applications in viral dynamics. *SIAM Review*, 53(1):3–39, 2011. doi:10.1137/090757009.

M. Scalise, L. Pochini, M. Galluccio, L. Console, and C. Indiveri. Glutamine transport and mitochondrial metabolism in cancer cell growth. *Frontiers in Oncology*, 7:1–9, 2017. doi:10.3389/fonc.2017.00306.

A. A. Shestov, X. Liu, Z. Ser, A. A. Cluntun, Y. P. Hung, L. Huang, D. Kim, A. Le, G. Yellen, J. G. Albeck, and J. W. Locasale. Quantitative determinants of aerobic glycolysis identify flux through the enzyme GAPDH as a limiting step. *eLife*, 3:e03342, 2014. doi:10.7554/eLife.03342.

J. D. Stigter and J. Molenaar. A fast algorithm to assess local structural identifiability. *Automatica*, 58:118–124, 2015. doi:10.1016/j.automatica.2015.05.004.

J. D. Stigter, M. B. Beck, and J. Molenaar. Assessing local structural identifiability for environmental models. *Environmental Modelling and Software*, 93:398–408, 2017. doi:10.1016/j.envsoft.2017.03.006.

A. F. Villaverde. Observability and structural identifiability of nonlinear biological systems. *Complexity*, 2019, 2019. doi:10.1155/2019/8497093.

O. Warburg. On the origin of cancer cells. *Science*, 123(3191):309–314, 1956. doi:10.1126/science.123.3191.309.

D. R. Wise and C. B. Thompson. Glutamine addiction: A new therapeutic target in cancer. *Trends in Biochemical Sciences*, 35(8):427–433, 2010. doi:10.1016/j.tibs.2010.05.003.